POLITECNICO
MILANO 1863

SCUOLA DI INGEGNERIA INDUSTRIALE
E DELL'INFORMAZIONE

EXECUTIVE SUMMARY OF THE THESIS

Integrated nuclear-solid oxide electrolysis systems for electricity and hydrogen production

TESI MAGISTRALE IN ENERGY ENGINEERING – INGEGNERIA ENERGETICA

AUTHOR: ADRIANO GIANCHINO

ADVISOR: DR. PAOLO COLBERTALDO

ACADEMIC YEAR: 2022-2023

1. Introduction

Climate change refers to the long-term shifts in temperature and weather patterns on a global scale, whose effects greatly impact life on Earth. This is linked to the large release of anthropogenic Greenhouse Gases (GHGs) in the atmosphere due to the use of fossil fuels. Multiple international treaties were signed in recent years, like the Paris Agreement in 2015, where 196 countries pledged to reduce GHGs emissions to limit the temperature increase to 1.5°C above pre-industrial levels.

Nuclear power plants (NPPs) and variable renewable energy sources (VRES) are valid alternatives of low-emission technologies, both with pros (baseload operation and wide availability, respectively) and cons (waste management and intermittency, respectively). Additional technologies are needed for the transition process, such as energy storage [1] and new energy vectors (e.g., hydrogen and clean fuels), for instance to tackle the hard-to-abate sectors (e.g., high-temperature industrial heat, aviation or marine transportation, and others) [2].

A high penetration of VRES could also compromise the electric grid operation and stability due to intermittency and absence of inertia, requiring other technologies to act in support to the electric grid needs [3].

In this context, the integration of sustainable hydrogen production using solid oxide electrolysis cells (SOECs) operating at 600-900°C [4] with electricity and heat generation in NPPs represents an interesting solution to some of these issues [5]. This type of integrated energy system (IES) would allow to operate the NPP at baseload on the thermal side, while also avoiding VRES curtailment when an excess is generated, by reducing the NPP output to the grid and using instead part of its heat and electricity to produce hydrogen, thus releasing an energy vector for storing energy in chemical form or for other uses. This is also expected to increase the overall system profitability [6], [7].

The use of small modular nuclear reactors (SMNRs) for this purpose would allow to cut costs related to hydrogen storage and transportation, reduce overall building time, reduce land use, enhance flexibility, establish potential synergies with VRES (helping to increase their penetration), and enable delocalized hydrogen production [8].

The possibility of hydrogen production through the integration of SMNR and SOEC has not been transferred into operational projects yet but has been studied numerically for some applications. The techno-economic feasibility is usually investigated by simulating the IES operation according to load curves for small islands [9] or towns [10]. The SMNRs are usually pressurized water reactors (PWRs) with an electrical power of around 300 MW_e and maximum temperature in the 300-320°C range ([9], [11]), but also very high temperature reactors (VHTRs) with temperatures in the 800-1000°C are studied [8].
The available works in literature, however, do not include accurate models for SMNRs and SOECs, and the adopted models do not deepen the analysis of the interaction between the two systems.
This thesis work investigates the feasibility of such an IES from a technical point of view. A model is developed, combining a representation of the power section of the NPP and a SOEC-based hydrogen production section.

2. Methods

The proposed integrated system includes a NPP powered by a SMNR, and a hydrogen production system based on solid oxide electrolysis cells (SOECs) and is schematized in Figure 2.1.

2.1. NPP power block

The SMNR is assumed to always work at design conditions. A steam bleeding from the NPP provides thermal power to the hydrogen system, while the electricity generated in the NPP is partially used to power the SOEC stack and the balance-of-plant components. The steam bleeding is placed downstream the steam generator (SG) (i.e., upstream of the high-pressure turbine, HPT), where temperature and pressure of the steam are at the maximum values. This superheated steam is used to provide thermal power to the hydrogen system, using it to perform water evaporation in a heat exchanger. Then, the stream from the NPP is sent to a heat recovery section before being returned to the NPP at the condenser.
This type of operation represents a novelty, and no data are available in scientific literature at best of knowledge of the author. This required to model the NPP power block (PB) to assess the effect of the variation of the bled fraction of the steam mass flow rate (ε) on the electric power generation.

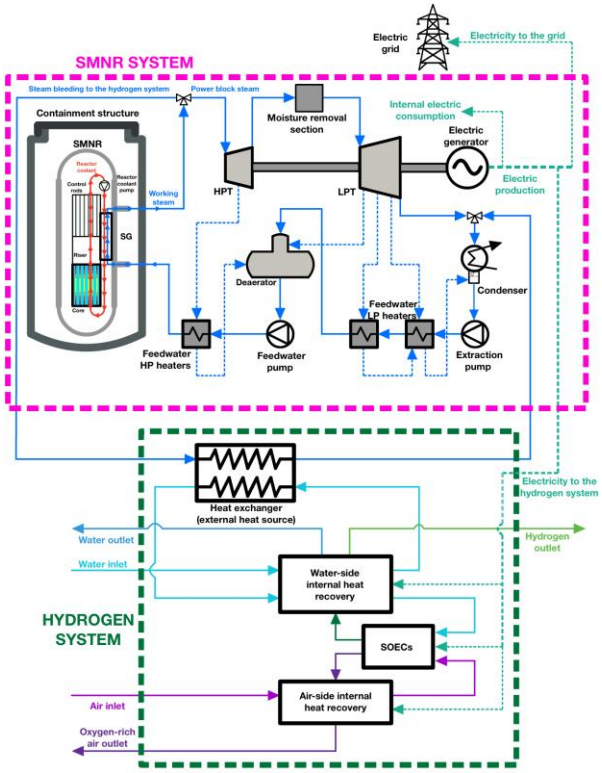

Figure 2.1 - Scheme of the integrated system.

The PB was modelled on THERMOFLEX® based on data for an IRIS plant [12], [13]. The main design quantities are shown in Table 2.1, which were obtained by simulating the operation of the PB starting from the design condition (ε=0%).

Table 2.1 - Main characteristics of the modelled SMNR

Steam mass flow rate [kg/s]	521.4
SG cold outlet/HPT inlet temperature [°C]	317
SG cold outlet/HPT inlet pressure [bar]	58
LPT inlet temperature [°C]	271
LPT inlet pressure [bar]	10.34
Available electric power [MW_e]	336.5
First-law efficiency [%]	32.43%

Then, off-design conditions at increasing values of ε were simulated, until the output electric power generation was null. An electric heater was added to the PB layout upstream the SG so to always maintain the design temperature at SG inlet, as a change would impact on the primary loop and therefore on the core, which is extremely sensitive to variations and assumed to work at constant power. This measure was required as the feedwater preheating line was unable to meet the design cold-side inlet temperature of the SG when ε increased. The power consumption of the electric heater reduces the availability of electric power from the NPP. A process of data fitting on the results allowed to find a cubic polynomial that expresses the available electric power from the

NPP (Q, [MW_e]) as a function of ε (m, [kg/s]) as shown in Figure 2.2.

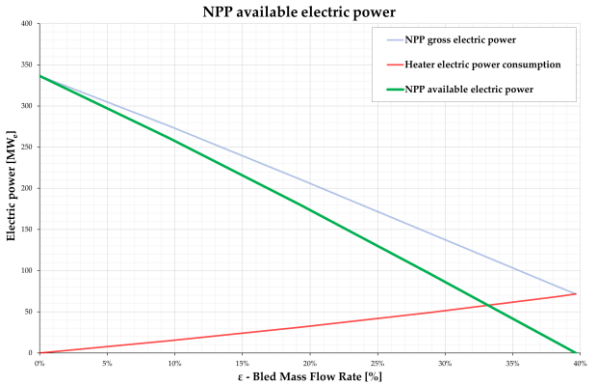

Figure 2.2- NPP available electric power as a function of ε

2.2. Hydrogen system design and operation

The hydrogen system was modelled on Aspen Plus®. The plant is composed of electrolysis modules, whose number was to be determined in the sizing process together with the size of the heat exchangers and the balance-of-plant components in each module.

A total of three different plant layouts were proposed (cases A, B, C), and both exothermic (option 1, [14]) and endothermic (option 2, [15]) operations were considered, for a total of six configurations.

In the layout for case A (Figure 3.1), no crossover between anode (purple lines) and cathode (green lines) streams for internal heat recovery is present. HX-SPIL is a heat exchanger that works as the interface between the NPP and the hydrogen system. Steam at 317°C and 58 bar is bled from the NPP and equally split among the modules, then is laminated at 5 bar to avoid large pressure gradients inside HX-SPIL (temperature drops to 260°C in the process), flows at the hot side of HX-SPIL where it is brought to saturated vapor conditions (to avoid phase change at both sides of HX-SPIL), then it is sent to a heat recovery section before being returned to the NPP condenser.

The cold-side inlet of HX-SPIL is subcooled water at 97°C from HX-PR-CA, this water is evaporated at around ambient pressure and superheated to 150°C. Outlet hydrogen is partially recirculated (MIX) to achieve a molar composition of 90% water and 10% hydrogen for the stack inlet stream.

The stacks are modelled as a chemical reactor (REACTOR) and a separator (SEP).

A utilization factor (UF) of 0.7 was imposed, meaning that 0.7 mol of hydrogen are generated for each mole of inlet water.

In case B, the crossover between anode and cathode is present, and anode outlet participates to internal heat recovery for water preheating at hot side of HX-PR-CA, while the cathode outlet stream is only responsible for inlet stream superheating (HX-HT-CA).

The difference between cases C and B is that HX-SPIL is sized at system-level for the former. Each of the six configurations was sized on the value of ε at which the electric power delivered to the grid was null (around ε=25%), and the most relevant quantities are reported in

Table 3.1. A preliminary analysis based on a few KPIs (last three lines of

Table 3.1) was carried out at design conditions, and case C was excluded as the rigidity of an HX- SPIL sized at system-level was not balanced by better performances with respect to the other cases. Then, an off-design steady-state simulation was carried out for the remaining four configurations.

The systems, sized in the previous step, were tested over the whole ε operating range (25% to 0%), which was divided into steps of 1% each, so to test the four configurations at the exact same value of ε at each step and carry out a fair comparison.

For each step of the ε range, the number of active modules was adjusted to find an operating point which fulfilled the requirements imposed for regulation (current density below 1 A/cm² to preserve cells durability and at least 10% of the nominal mass flow rates flowing at any section to avoid problems with circulation and pressure drops). The number of active modules at each step was kept as high as possible for configurations A1 and B1 (exothermic), as keeping current density (j) below the design value (0.8 A/cm²) was beneficial for the system performances since the operating point moved closer to the thermoneutral condition. For cases A2 and B2 (endothermic), operation at j higher than design was beneficial for the same reason, but lower values were favored (when possible) to enhance cells durability, as too high values of j are detrimental for this aspect.

3. Results and discussion

The data at each valid operating point found for each configuration were extracted, allowing to build an operating map of the integrated system.

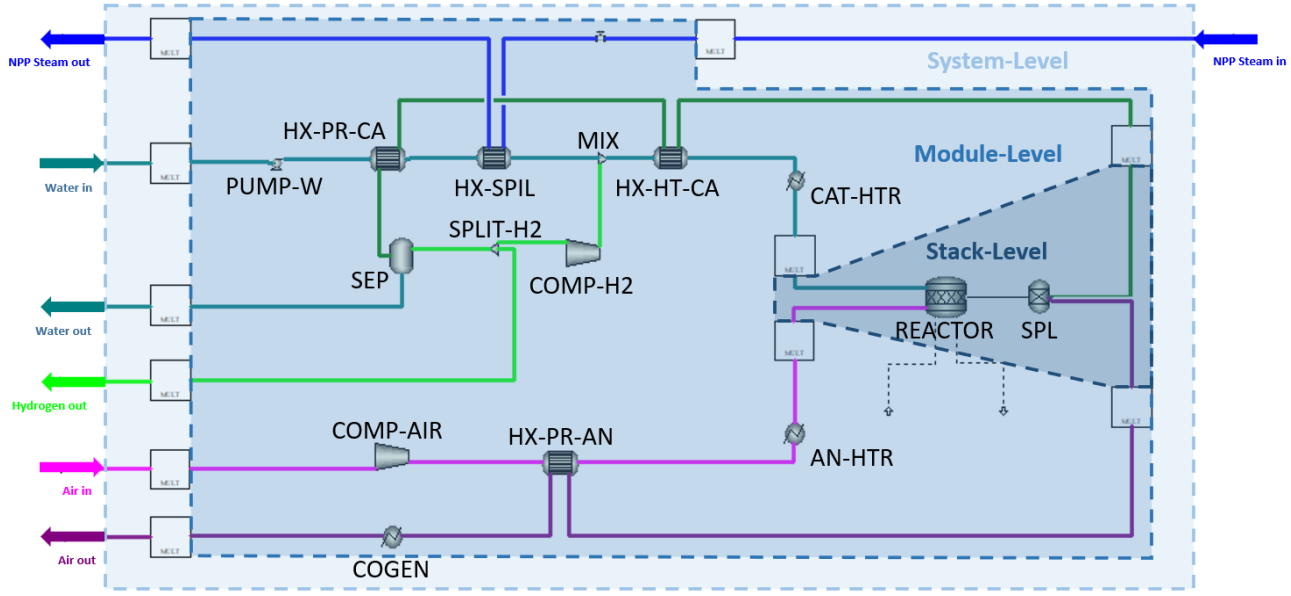

Figure 3.1 - Hydrogen system layout for case A

Table 3.1 - Significant quantities at design conditions for the six proposed configurations

Physical quantities	Exothermic configurations			Endothermic configurations		
	A1	B1	C1	A2	B2	C2
Modules in the system	18	18	18	18	18	18
Total cells in the system	270,000	270,000	270,000	270,000	270,000	270,000
V_{cells} [V]	1.385	1.388	1.388	1.0396	1.0376	1.0376
j_{cells} [mA/cm²]	0.791	0.796	0.796	0.7952	0.7870	0.7872
ε_{design}	25.3%	25.5%	25.5%	25.5%	25.2%	25.2%
System electric power at design, $W_{el,sys}$ [MW_e]	127.286	125.896	125.889	126.049	128.431	128.501
Stack electric efficiency	90.5%	90.3%	90.3%	120.5%	120.8%	120.8%
Module electric efficiency	84.1%	85.5%	85.5%	85.4%	82.9%	82.9%
Module first-law efficiency	68.8%	69.8%	69.8%	69.7%	68.1%	68.0%

It is important to highlight that since the active modules are always imposed to work in the same way, the overall system performances coincide with the one for single active module, and the absolute quantities at system level (like powers and mass flow rates) can be obtained multiplying the ones for an active module by the number of active modules.

3.1. Hydrogen production

Since the four configurations use the same exact logic to regulate inlet water according to ε, and UF is imposed and equal and kept constant, the mass flow rate of hydrogen produced by the system was roughly the same for all four configurations, with minor differences due to the equal number of cells in the system for slightly different values of design ε, reflected by slightly different voltages at design for cases A1-B1 and A2-B2, respectively (Table 3.1).

Hence, this parameter is not enough to discriminate one configuration over the others.

3.2. Stack electric efficiency

The stack electric efficiency was around 40% higher for the endothermic configurations (A2, B2), as expected from SOEC theory, as this operating mode allows to offset part of the electricity needed for electrolysis with heat. This allows the endothermic configurations (A2, B2) to reach stack electric efficiencies of around 120%, while exothermic configurations (A1, B1) must entirely rely on electricity to perform electrolysis and reach a stack electric efficiency of around 90%.

3.3. Module electric consumption

Extending the analysis to the whole module, the benefit from better stack electric efficiency for configurations A2 and B2 was cancelled and even overturned. This phenomenon can be addressed to

the values of operating cell voltage for the different configurations.
Indeed, A2 and B2 operate in a range of cell voltages relatively further from thermoneutral with respect to A1 and B1. This implies that larger quantities of heat in absolute value are involved in electrolysis for endothermic cases. This greater amount of heat requires larger air mass flow rates at anode-side of the stacks to keep the delta of temperature between stack inlet and outlet as constant as possible.
Moreover, given that A2 and B2 are operating in endothermic conditions, stack outlet temperature is lower than inlet (
Table 3.1), meaning that internal heat recovery in the hydrogen system is not enough for inlet streams to reach the design stack inlet temperature. This imposes the use of electric heaters placed upstream the stacks (CAT-HTR and AN-HTR in Figure 3.1), which must top up the temperature. The electric consumption of these electric heaters has a significant impact on the module electric power consumption, which is higher for endothermic configurations.
The electric power consumption of the machines in the module (PUMP-W, COMP-H2 and COMP-AIR in Figure 3.1) is negligible over the total module electric consumption, which mostly consists of the electric power used by the stacks and, secondly, from the electric heaters when operating (always, for A2 and B2).

3.4. Module first-law efficiency

Figure 3.2 shows how the modules first-law efficiencies vary on the operational range (solid lines): this quantity is the ratio between the thermal power potentially achievable from the produced hydrogen (LHV) and the sum of the module electric and thermal power consumption.
The columns at the bottom of the figure represent the active modules along the operational range. It is evident how the strategies introduced in section **Errore. L'origine riferimento non è stata trovata.** affect the number of active modules for a given ε according to the considered configuration.
Overall, configurations A1-B1 show higher first-law efficiencies with respect to endothermic (A2, B2) as their lower module power consumption is enough to overturn the lower electric power consumption of the stacks in A2 and B2.
The sawtooth-like profiles of the trends for A1 and B2 are caused by the larger variation in operative voltage for these configurations due to the higher slope of the polarization curve with respect to that used for A2 and B2.

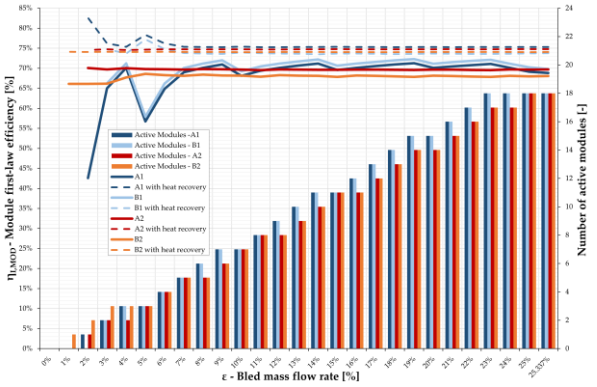

Figure 3.2- Module first-law efficiency over the operational range

This causes A1 and B1 to operate in a wider band of cell voltages for the same variation in current density with respect to A2 and B2, causing a relatively greater shift from thermoneutral and, consequently, a larger variation in air mass flow rate. These variations cause the power consumption of the module to fluctuate accordingly, explaining the sawtooth-like profile for A1-B1 and the smoother trend for A2-B2. This phenomenon for becomes even more pronounced for exothermic configurations when ε is low and the operating modules are fewer.
Due to the constraints imposed to determine the number of active modules, a valid working condition was found at ε=5% for a number of modules which caused current density (and hence, voltage) to increase, moving the operating point further from thermoneutral, increasing the heat released in the process. The consequential increase in air mass flow rate caused the anode-side heat exchanger (HX-PR-AN in Figure 3.1) to become undersized and unable to meet the specifications for stack inlet temperature.
This caused AN-HTR to become operational and its electric power consumption to spike, increasing the module power consumption.
Since the produced hydrogen linearly depends on ε (and hence, since UF is constant, on inlet water), the increase in the module power consumption was not accompanied by an increased hydrogen production, causing the first-law efficiency for A1 and B1 to drop to around 56%, resulting in a deep indentation in the blue lines. For the same reason, first-law efficiency for configurations A1 and B1 plunges below 45% at even lower values of ε, where the described effect is even stronger. Due to

the large power consumption related to external electric heaters for configurations A2 and B2, endothermic operation reduces the overall system efficiency when coupled with a heat source with temperatures lower than the one at stack inlet.
Increasing the layout complexity with hot streams crossover (cases B) only slightly increases the efficiency. As the hydrogen system is not very sensible to the layout variation, the simpler exothermic configuration could be preferred (configuration A1).
Lastly, it is evident that only configuration B2 has a working point at ε=1%, as configurations A1 and A2 stop at 2%, while B1 at 3%.
This is because it was impossible to find a working point for any number of active modules able to satisfy the constraints on the modules operations (section 2.2), forcing the hydrogen system shut down despite the availability of heat and electricity from the NPP.
The sensitivity of exothermic configurations to the adopted regulation strategy suggests that it could be worth to investigate an asymmetrical operation of the active modules to smooth the efficiency trend. Moreover, the large efficiency fluctuations and high current density values at low ε may suggest starting to operate the hydrogen system at higher values, reducing of the power delivered to the grid in that region only with NPP regulation.
The dashed lines in Figure 3.2 represent the first-law efficiencies considering heat recovery from the hot outlet streams as a useful product of the plant, as it could be used for other applications like low-pressure steam or sanitary hot water production. In this context, as hydrogen is the main product of the system, this efficiency provides an expression of how well the system is using the heat in the circulating streams.
Indeed, its value increases when heat is not directly involved in the electrolysis process (hence, more is available for recovery). This is clear when looking at the lines for configurations A1 and B1 in the region around ε=5%. As it was explained, the increase in the circulating streams heat in this region does not strictly affect hydrogen production, which is just less efficient.
Moreover, this heat cannot be fully recovered due to the undersized heat exchanger, causing an increase in heat rejection from the outlet streams (and hence, a decrease in first-law efficiency). The peak in the first-law efficiency with heat recovery of configurations A1 and B1 can be addressed in the same way to the already-discussed plunge in the respective first-law efficiencies.
The module-level efficiencies perfectly coincide with those at system-level as all the active modules operate symmetrically.

3.5. Integrated system

Figure 3.3 shows the Sankey diagram for the integrated NPP-SOE system using configuration A1 at around half the operational range (ε=11%). It is evident how inefficient the use of the thermal power from the NPP bled steam is, as most of it is not exploited in the hydrogen plant and is sent to heat recovery.

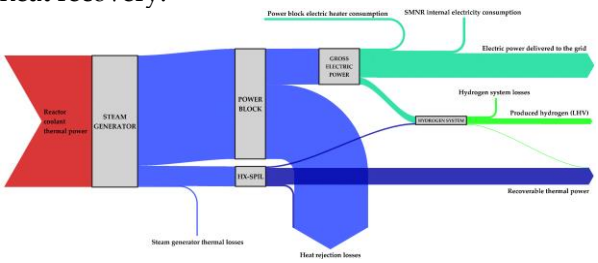

Figure 3.3 - Sankey diagram for configuration A1 at ε=11%

This is because only the heat recovered from steam desuperheating is actively used by the hydrogen system, as explained in section 2.2. However, this only represents 10% of the available thermal power, as most of it can be recovered by condensing the bled mass flow rate (80%), as shown by the thicker dark blue line in the figure.
Moreover, the power consumption related to the electric heater in the NPP power block significantly reduces the availability of electric power from the NPP. The power availability reduction due to the electric heater increases with ε, as shown in Figure 2.2.

4. Conclusions

This thesis analyzed the integration of a SMNR-NPP with an electric nominal power of 336.5 MW_e with a hydrogen production system based on solid oxide electrolysis. The work involved the development of two models, on Thermoflex and Aspen Plus, respectively.
The analysis highlighted how the NPP is able to provide electricity even for mass flow rates of steam bled upstream the HPT up to 39.7% of the nominal at the cold side of the SG. The availability of electric power in off-design operation is significantly reduced by the PB electric heater consumption (around 72 MW_e at ε=39.7%).

The hydrogen system is able to operate both with exothermic and endothermic stacks, with electric efficiencies of around 90% and 120%, respectively. The values for first-law efficiencies are closer, with values around 67.5-70% for endothermic stacks and 70-72.5% for exothermic stacks. The maximum difference between first-law efficiencies for the two cases is around 4.5 percentage points, with the exothermic configurations having the higher values.

Off-design operation of the hydrogen system did not show significant challenges for values of ε between 7% and design (around 25%). For lower values of ε, the operation became more complex and required trade-offs due to the imposed constraints. Configuration B2 (endothermic case with outlet streams crossover) showed the largest operational range, being able to operate down to ε=1%, while the other configurations required an earlier shut down at ε=2-3%, which is still an interesting range. The first-law efficiency was almost constant on all the operative range for endothermic cases, while in endothermic cases it was strongly affected by the electric heaters power consumption for values of ε below 7%, with fluctuations in the order of 13-27 percentage points.

The decision to avoid a double phase change in NPP-SOEC heat exchanger greatly increases the share of available thermal power from the bled steam downstream the component, as only 10% is used to perform water evaporation and 80% is sent to the heat recovery section. This factor strongly impacts on the overall IES efficiency.

As the NPP power block is sensitive to the reduction of circulating steam mass flow rate, the steam bleeding point could be moved to the LPT inlet, allowing the HPT to work at nominal mass flow rate. A suitable bleeding point is upstream the LPT inlet, where the values of pressure and temperature are still perfectly compatible with the HX-SPIL operation.

References

[1] M. M. Rahman, A. O. Oni, E. Gemechu, and A. Kumar, "Assessment of energy storage technologies: A review," *Energy Conversion and Management*, vol. 223. Elsevier Ltd, Nov. 01, 2020. doi: 10.1016/j.enconman.2020.113295.

[2] International Energy Agency (IEA), "Understanding GEC Model Scenarios." [Online]. Available: https://www.iea.org/reports/global-energy-and-climate-model/understanding-gec-model-scenarios

[3] K. Guerra, P. Haro, R. E. Gutiérrez, and A. Gómez-Barea, "Facing the high share of variable renewable energy in the power system: Flexibility and stability requirements," *Appl Energy*, vol. 310, Mar. 2022, doi: 10.1016/j.apenergy.2022.118561.

[4] S. Shiva Kumar and H. Lim, "An overview of water electrolysis technologies for green hydrogen production," *Energy Reports*, vol. 8. Elsevier Ltd, pp. 13793–13813, Nov. 01, 2022. doi: 10.1016/j.egyr.2022.10.127.

[5] Nuclear Energy Agency (NEA), "The Role of Nuclear Power in the Hydrogen Economy - Cost and Competitiveness," 2022.

[6] R. S. El-Emam and M. H. Subki, "Small modular reactors for nuclear-renewable synergies: Prospects and impediments," *Int J Energy Res*, vol. 45, no. 11, pp. 16995–17004, Sep. 2021, doi: 10.1002/er.6838.

[7] International Energy Agency (IEA), "Hydrogen Production and Infrastructure Projects Database." [Online]. Available: https://www.iea.org/data-and-statistics/data-product/hydrogen-production-and-infrastructure-projects-database#hydrogen-production-projects

[8] J. M. Lee *et al.*, "Environ-economic analysis of high-temperature steam electrolysis for decentralized hydrogen production," *Energy Convers Manag*, vol. 266, Aug. 2022, doi: 10.1016/j.enconman.2022.115856.

[9] N. Chalkiadakis, E. Stamatakis, M. Varvayanni, A. Stubos, G. Tzamalis, and T. Tsoutsos, "A New Path towards Sustainable Energy Transition: Techno-Economic Feasibility of a Complete Hybrid Small Modular Reactor/Hydrogen (SMR/H2) Energy System," *Energies (Basel)*, vol. 16, no. 17, Sep. 2023, doi: 10.3390/en16176257.

[10] A. Ho, K. Mohammadi, M. Memmott, J. Hedengren, and K. M. Powell, "Dynamic simulation of a novel nuclear hybrid energy system with large-scale hydrogen storage in an underground salt cavern," *Int J*

Hydrogen Energy, vol. 46, no. 61, pp. 31143–31157, Sep. 2021, doi: 10.1016/j.ijhydene.2021.07.027.

[11] J. S. Kim, R. D. Boardman, and S. M. Bragg-Sitton, "Dynamic performance analysis of a high-temperature steam electrolysis plant integrated within nuclear-renewable hybrid energy systems," *Appl Energy*, vol. 228, pp. 2090–2110, Oct. 2018, doi: 10.1016/j.apenergy.2018.07.060.

[12] M. D. Carelli, B. Petrović, N. Čavlina, and D. Grgić, "IRIS (International Reactor Innovative and Secure)-Design Overview and Deployment Prospects," Bled, Slovenia, Sep. 2005.

[13] M. Williamson and L. Townsend, "Sizes of Secondary Plant Components for Modularized IRIS Balance of Plant Design," 2003.

[14] L. Barelli, G. Bidini, G. Cinti, and A. Ottaviano, "Study of SOFC-SOE transition on a RSOFC stack," *Int J Hydrogen Energy*, vol. 42, no. 41, pp. 26037–26047, Oct. 2017, doi: 10.1016/j.ijhydene.2017.08.159.

[15] M. Reytier *et al.*, "Stack performances in high temperature steam electrolysis and co-electrolysis," in *International Journal of Hydrogen Energy*, Elsevier Ltd, Sep. 2015, pp. 11370–11377. doi: 10.1016/j.ijhydene.2015.04.085.